High-resolution diffusion-weighted imaging of the breast with multiband 2D radiofrequency pulses and a generalized parallel imaging reconstruction

Valentina Taviani, PhD[1], **Marcus T. Alley, PhD**[1], **Suchandrima Banerjee, PhD**[2], **Dwight G. Nishimura, PhD**[3], **Bruce L. Daniel, MD**[1], **Shreyas S. Vasanawala, MD, PhD**[1], **Brian A. Hargreaves, PhD**[1]

[1]Department of Radiology, Stanford University, Stanford, California, USA

[2]Global Applied Science Laboratory, GE Healthcare, Menlo Park, California, USA

[3]Department of Electrical Engineering, Magnetic Resonance Systems Research Laboratory, Stanford University, Stanford, California, USA

Abstract

Purpose: To develop a technique for high-resolution diffusion-weighted imaging (DWI) and to compare it to standard DWI methods.

Methods: Multiple in-plane bands of magnetization were simultaneously excited by identically phase modulating each sub-pulse of a 2D RF pulse. Several excitations with the same multiband pattern progressively shifted in the phase-encode direction were used to cover the prescribed FOV. The phase-encoded FOV was limited to the width of a single band to reduce off-resonance-induced distortion and blurring. Parallel imaging (PI) techniques were used to resolve aliasing from the other bands and to combine the different excitations. Following validation in phantoms and healthy volunteers, a preliminary study in breast cancer patients (N=14) was performed to compare the proposed method to conventional DWI with PI and to reduced-FOV DWI.

Results: The proposed method gave high-resolution diffusion-weighted images with minimal artifacts at the band intersections. Compared to PI alone, higher phase-encoded FOV-reduction factors and reduced noise amplification were obtained, which translated to higher resolution images than conventional (non-multiband) DWI. The same resolution and image quality achievable over targeted regions using existing reduced-FOV methods was obtained, but the proposed method also enables complete bilateral coverage.

Conclusion: We developed an in-plane multiband technique for high-resolution DWI and compared its performance to other standard DWI methods.

Keywords

DWI; multiband; 2D RF pulse; parallel imaging; breast

Address for correspondence: Valentina Taviani, 1201 Welch Road, Stanford, CA 94304, Phone: 617-415-8202, taviani@stanford.edu.

Introduction

Diffusion-weighted imaging (DWI) is emerging as a promising non-contrast technique to increase the specificity of current breast MRI protocols (1,2). Recent studies have shown a reduction of false positives and associated morbidity when breast DWI is used together with dynamic contrast-enhanced MRI (3). Single-shot diffusion-weighted echo planar imaging (EPI) is commonly used because of its robustness to motion and high signal to noise ratio (SNR) efficiency. However, the long echo-train readout and narrow effective readout bandwidth in the phase encode (PE) direction make this technique extremely sensitive to T2* induced decay (blurring) and off-resonance, with field inhomogeneities, susceptibility gradients, eddy currents and chemical shift often resulting in severe geometrical distortion. The need for bilateral coverage and high in-plane resolution make DWI of the breast particularly challenging, especially at 3T, where the increased sensitivity to off-resonance and B1 inhomogeneity cause increased anatomical distortion and shading.

Several high-resolution DWI methods based on echo-planar trajectories have been developed that maximize the velocity of k-space traversal in the PE direction to limit distortion and blurring while preserving resolution (4–11). Parallel imaging is used extensively with DWI to reduce blurring and distortion due to the EPI readout (4,12); however, noise amplification and residual aliasing limit practical acceleration factors. In multi-shot methods, only a subset of k-space lines is acquired following each diffusion-sensitizing period, so that several acquisitions are necessary to fully encode k-space. Additional navigator data (5,7,8,13) or carefully designed, self-navigated trajectories (9,11) are therefore necessary to correct for shot-to-shot phase inconsistencies caused by physiological and bulk motion. Despite their complexity, the small phase-encoded FOV and short echo spacing achievable with these techniques have been shown to provide excellent resolution and anatomical fidelity (5).

Single-shot EPI has been used in conjunction with outer volume suppression pulses (14–17), inner volume excitation (18–20) and 2D spatially selective radiofrequency (RF) excitation pulses (21) for high-resolution imaging of targeted regions. These methods enable faster k-space traversal in the PE direction by reducing the phase-encoded FOV during acquisition and have been successfully used for imaging the spine (22), prostate (23–25), pancreas (26,27), kidneys (28) and thyroids (29), as well as for treatment monitoring in the breast (30,31). Due to their limited coverage these techniques are unsuitable for screening purposes and inadequate for many other diagnostic applications. Other groups have recently explored strategies to perform image-space combination of a series of reduced-FOV images consecutively acquired to cover the desired FOV (32). Estimates of the excitation profiles and generalized parallel imaging reconstruction techniques have been shown to allow smooth combination of contiguous volumes with minimal overlap (33). The main limitation of these methods is that they require a large number of acquisitions to cover the prescribed FOV, which severely limits their applicability outside the brain, where much larger FOVs are often used.

In this work we propose a method for high resolution DWI that combines reduced-FOV imaging, 2D selective in-plane multi-band excitation and a generalized parallel imaging reconstruction method to extend the high-resolution and high anatomical fidelity achievable

with reduced-FOV imaging over the much larger FOVs required for bilateral breast exams. Phantom experiments, as well as *in vivo* experiments in healthy volunteers and patients, were performed to assess feasibility of the proposed technique.

Methods

The shorter echo train length (ETL) allowed by reduced-phase-encoded-FOV methods results in faster k-space traversal and therefore lower distortion and T2*-induced blurring for a given resolution. In this work we use a 2D RF pulse to limit the excited FOV to a narrow band of magnetization and then acquire with phase encoding along the shortest dimension and phase-encoded FOV set to cover the width of the excited band, as in ref (21). By phase modulating the individual sub-pulses, multiple in-plane bands can be excited simultaneously (Figure 1a). As the phase-encoded FOV covers the width of a single band, simultaneously excited bands will fold over. However, if the distance between the bands is comparable to the distance between the physical receiver elements of a multichannel array coil, signals originating from different excited bands can be resolved using parallel imaging (Figure 1b). The desired anatomical coverage is obtained by sweeping the multiband (MB) excitation pattern in the PE direction (different colors in Fig.1b) to cover the space between bands. Since both excitation profiles and coil-sensitivity profiles both multiply the received signal, the signals from each coil and each excitation pattern are treated as separate channels. A generalized parallel imaging strategy (with specifically designed calibration procedure) is thus used to resolve signals originating from simultaneously excited bands while efficiently combining different strips of magnetization into a composite image with minimal boundary artifacts between adjacent bands. Details of the MB 2D RF pulse, pulse sequence, calibration and reconstruction are provided in the following sections.

Multiband 2D RF pulse

The 2D echo-planar RF pulse used in this work was similar to that described in ref. (21). A 90° flip angle was generated over a 4 cm slab of magnetisation and the specified slice thickness. The fast echo-planar direction during excitation corresponded to the PE direction during imaging. A time-bandwidth (TBW) product of 6 in the PE direction resulted in minimal aliasing from transition bands when combined with a phase-encoded FOV of 4cm. The slow ("blipped") direction of the excitation was in the slice-select (SS) direction, resulting in multiple simultaneously excited slices (periodic excitation side lobes) and a shift of the fat excitation profile in the SS direction with respect to the water signal (cfr. Figure 1a). The pulse was designed with bandwidth under 220 Hz so that no overlap existed between the fat and water slice-direction profiles for B_0 1.5T (42 sub-pulses, 376us each, $TBW_{SS} = 3.1$). A 180° refocusing pulse (pulse width = 3.6ms; BW = 806Hz) used in conjunction with the 2D RF pulse ensured refocusing of the main lobe of the periodic 2D excitation while suppressing fat (21). The duration of the 2D RF pulse (16.6ms) was minimised by transmitting during both gradient polarities. In-plane MB excitation patterns were obtained by summing multiple 2D RF pulses after linear phase modulation of the individual sub-pulses. Three bands at a time could be excited with a peak B1 of 19 μT.

Pulse sequence

Diffusion encoding gradients were played out immediately before and after the 180° refocusing pulse. A Stejskal-Tanner diffusion encoding scheme with gradients simultaneously played on all 3 axes was used to minimize TE for a given b value. A conventional half-Fourier EPI readout with 24 lines on the non-fully-sampled side of k_y was used to further reduce TE. Ramp sampling and the maximum readout gradient amplitude (50 mT/m) were used to minimize the echo spacing (ESP). The phase-encoded FOV was controlled by the "FOV-reduction factor", defined as the ratio between reconstructed and effectively encoded FOV.

The acquisition consisted of a reference scan with phase encoding blips turned off, and the actual acquisition, which consisted of several passes with the MB excitation pattern progressively shifted in the PE direction. The number of passes depends on the desired phase-encode-direction FOV and the number of bands simultaneously excited, which in turn depend on the specific geometry of the multichannel array coil used for signal reception. In the breast, coil sensitivities vary the most in the right-left direction. With a 16-channel array coil and 3 simultaneously excited (4 cm) bands, assuming a 20% overlap between consecutive bands, four passes were required to cover a 38cm FOV. The blipped slice-direction excitation leads to slice sub-lobes that limit the maximum number of slices per TR to as many as can fit within two adjacent side lobes (16 slices). To acquire more than 16 slices, two acquisitions were performed.

Calibration

In conventional image-based parallel imaging, a fully sampled, low-resolution, proton-density acquisition is used to measure sensitivity maps. Here the sensitivity of multichannel coils and the spatially localized selectivity provided by the MB excitation pattern effectively complement each other. In the proposed framework, if Nc is the number of physical receiver coils and Np is the number of passes necessary to sweep the prescribed FOV, with each pass having a unique MB excitation pattern, the total number of "virtual" coils is $Nc \times Np$. Similarly to conventional imaged-based parallel imaging, "virtual" coil sensitivity maps are measured by performing a low resolution, fully sampled EPI calibration scan with the same MB excitation pattern and the same number of passes used for the actual acquisitionThe ESP used for calibration is reduced by the same reduction factor applied to the imaging FOV in the actual scan. While this is often possible and allows exact matching of the rates of k-space traversal between calibration and actual acquisition, there are cases when perfect matching cannot be achieved (e.g., low resolution and FOV-reduction factors) that could potentially result in reconstruction errors.

Both image-space (SENSE (34)) and k-space-based (ARC (35)) parallel imaging reconstructions were explored. ARC is a data-driven parallel imaging approach similar to GRAPPA (36). Because the same MB 2D RF pulse described above is used to acquire the calibration data, fat is inherently suppressed. With SENSE, to avoid inaccurate sensitivity map estimation in the low SNR regions resulting from fat suppression, the same calibration scan was repeated at the fat frequency and combined with the corresponding data at the water frequency to estimate sensitivity maps. In addition, sensitivity maps were normalized

using full-excitation-FOV images (i.e., single-band 2D excitation covering the prescribed FOV) acquired as part of the calibration procedure. This avoids artifacts that would occur at the intersection between adjacent bands when taking the sum of squares of the individual "virtual" coil images, due to the sharp transition regions in the MB excitation profile. The total calibration duration required for image-based parallel imaging was $(2 \times Np + 2) \times$ TR (about 30s for TR = 3s and 4 passes). With ARC, a single MB, multi-pass calibration scan performed at the water frequency was sufficient to acquire a pseudo "auto-calibration" region. The total calibration duration required for k-space-based parallel imaging reconstruction was $Np \times$ TR (about 12s for TR = 3s and 4 passes).

Image reconstruction

Step 1: EPI Phase correction and ramp sampling correction of calibration data
—Zero- and first-order phase correction terms to remove Nyquist ghosts were estimated using an iterative, entropy-driven minimization technique to avoid acquiring a separate reference scan for the calibration data (37). After phase correction, gridding of the non-uniform k-space data resulting from ramp sampling was performed. Phase and ramp sampling corrections were performed separately for all calibration datasets (4 datasets for image-based, a single dataset for k-space-based parallel imaging reconstruction).

Step 2: Sensitivity maps estimation—This step was required for image-based parallel imaging reconstruction only. All the calibration datasets (MB and full-excitation-FOV at the water and fat frequency) were inverse Fourier transformed and interpolated to the same resolution of the actual acquisition after summation of the corresponding water and fat data. Sensitivity maps were estimated by dividing each "virtual coil" image by the corresponding coil-combined (sum of squares), full-excitation-FOV image, similarly to conventional SENSE reconstruction where each coil image is divided by the sum of squares of all the coil images. Regions containing pure noise were identified by thresholding and density filtering of the coil-combined full-excitation-FOV image. An extrapolation region was defined by region growing.

Step 3: Phase correction and ramp sampling correction of accelerated data—Phase correction (Nyquist ghost removal) of the accelerated data was performed by applying zero- and first-order phase terms derived from the reference scan data to every k-space line. Phase correction coefficients were obtained on a coil-by-coil basis, and those from the channel with the highest SNR were applied to all receivers. Ramp sampling correction was performed by conventional gridding of each acquired echo following phase correction.

Step 4: Parallel imaging and partial Fourier reconstruction—Homodyne reconstruction removes all image phase, including that from the receive B1 field. A generalized SENSE reconstruction with partial Fourier homodyne reconstruction similar to that described in ref. (38) was used to preserve the B1 field phase so that the unaliased spin distribution could be recovered before phase removal by homodyne detection. Each acquisition (signal average) was reconstructed separately.

k-space based parallel imaging reconstruction (ARC) and partial Fourier reconstruction can be effectively decoupled. Each acquisition (signal average) was reconstructed using ARC (kernel size = 2×FOV-reduction factor; regularization factor = 0.001), followed by conventional homodyne reconstruction. Homodyne removes the slowly varying image phase that could include unwanted terms due to motion occurring during the diffusion-sensitizing period. Real-valued averaging was performed for each b value for both SENSE and ARC reconstructions to minimize the noise bias that would result from magnitude averaging.

Phantom experiments

Imaging was performed on a 3T whole-body GE MR750 system (maximum gradient strength = 50mT/m; maximum slew rate = 200mT/m/ms). A simple spin-echo acquisition was used to illustrate the in-plane multiband excitation and generalized parallel imaging reconstruction without the complicating factors inherent to EPI (phase correction, gridding, distortion). The purpose of these experiments was: 1. to show that multiple MB excitation patterns allow undersampled datasets to be reconstructed using a generalized parallel imaging approach, even when only a single channel coil is available, and 2. to show that conventional parallel imaging in conjunction with multiple MB excitation patterns allows higher undersampling factors than parallel imaging alone.

Spin-echo images (TR = 300ms, TE = 14ms, FOV = 24cm, slice thickness = 5mm, matrix size = 256×256, bandwidth (rBW) = 15.6kHz) of a cylindrical resolution phantom were acquired using a single-channel, transmit/receive and an 8-channel, receive-only head coil. "Virtual" coil images were obtained by multiplying each coil image by the simulated excitation profile produced by the MB 2D RF pulse described above. MB factors of 2 and 3 (i.e. 2 and 3 coplanar bands, progressively shifted by (FOV-FWHM)/(Nb-1) each time, to cover the whole FOV, where FWHM is the full width at half maximum and Nb is the total number of excited bands) were simulated (distance between adjacent bands = 11.3cm and 7.6cm, respectively), together with undersampling factors ranging between 2 and 16. Images were reconstructed using the generalized SENSE approach described previously, with sensitivity maps obtained from the simulated excitation profiles. For multi-channel datasets, conventional sensitivity maps, calculated by dividing each low-resolution coil image (obtained by low-pass filtering the corresponding k-space data) by the sum of squares of all coil images, were multiplied by the simulated excitation profiles to obtain $Nc \times Np$ sensitivity maps. For single-channel data, the Np MB excitation profiles were used as sensitivity maps.

g-factor maps for both the standard and virtual coil configurations of an 8-channel bilateral breast coil (GE Healthcare) were computed using the pseudo multiple replica method (39). A dedicated breast phantom provided by the manufacturer was used to load the coil. For the standard coil configuration, a conventional b=0 single-shot DWI acquisition with full FOV excitation was used. The virtual coil configuration corresponded to a b=0 multiband acquisition with 3 coplanar bands simultaneously excited. The geometrical characteristics of the multiband excitation pattern as well as the imaging parameters used for both acquisitions were identical to those used for the preliminary patient study described below except for a matrix size of 256×256 and a FOV reduction factor of 4. These parameters were chosen to

keep distortion similar to that of the patient study while maintaining the same ratio between the effective undersampling factor and the number of physical receiver coils in the phase-encode direction. Both datasets were reconstructed using ARC.

In vivo imaging

Healthy volunteers were scanned using a 16-channel bilateral array coil (Sentinelle Medical, Inc, Toronto, ON, Canada). A MB factor of 3 (i.e. 3 simultaneously excited bands; distance between adjacent bands = 12.8cm; 4 passes; 3.2cm increment between consecutive passes) was used to acquire three datasets with progressively higher resolution while maintaining the same level of distortion and blurring. All datasets shared a 40cm FOV and 16 4mm-thick axial slices. Matrix sizes of 256^2, 382^2 and 512^2 were used for the first, second and third dataset respectively, with corresponding undersampling factors R = 4, 6 and 8. Other imaging parameters, common to all datasets were: TE = 55ms, TR = 3000ms, ETL = 40 (8 extra k-space lines for partial Fourier), b values = 0 (8 signal averages) and 600s/mm^2 (16 signal averages). In-plane resolutions of 1.56^2, 1.00^2 and 0.78^2 mm^2 were obtained. The total acquisition time was the same for all datasets (4min. 50sec.). For comparison, the first dataset was reconstructed using both SENSE and ARC. As our implementation of ARC gave better image quality than SENSE, while requiring a much faster calibration, the remaining datasets were reconstructed using ARC only. Corresponding full-excitation-FOV images with the same imaging parameters were acquired for comparison.

Preliminary comparative study in patients

Fourteen patients (24–68 years old; mean: 44.2; std: 13.0) with suspicious untreated breast abnormalities corresponding to known or suspected breast cancer were recruited for research MRI. A firm diagnosis for all lesions was established by core biopsy before or after MRI, or by surgical excision after MRI. Lesion types included invasive ductal carcinoma, infiltrating lobular carcinoma, ductal carcinoma in situ, fibroadenoma, ductal and pseudoangiomatous stromal hyperplasia, intraductal papillomas, sclerosing adenosis and seroma. All subjects who participated in the study gave written informed consent. Approval from the local institutional ethics board (Institutional Review Board) was obtained. A16-channel bilateral breast coil (Sentinelle Medical, Inc, Toronto, ON, Canada) was used. The protocol included 3D T1 spoiled gradient echo (SPGR), 3D T2 fast spin echo and dynamic contrast-enhanced 3D T1 SPGR (DISCO: DIfferential Subsampling with Cartesian Ordering, (40)) in addition to reduced FOV, conventional bilateral and multiband DWI. All diffusion scans were performed before contrast injection. Imaging parameters were set to test the hypothesis that the proposed MB technique can achieve the same image quality and same high resolution of clinically available reduced-FOV DWI methods, but with whole bilateral coverage. A $0.78\times0.78\times4$mm^3 resolution was obtained with the proposed MB method (MB factor=3, 4 passes to cover a 40cm FOV, distance between adjacent bands = 12.6cm, 512×512 matrix size, 8× undersampling factor, TE = 55ms, TR = 3000ms) and reduced-FOV DWI (10×5cm^2 FOV, 128×64 matrix size, TE = 51ms, TR = 3000ms). Conventional DWI with a resolution of $1.3\times1.3\times4$mm^3 was performed for comparison using the clinical protocol routinely used at our institution (34cm FOV, 256×256 matrix size, 4× parallel imaging acceleration, TE = 92ms, TR = 3000ms). Two b values, b=0 (8 signal averages) and b = 600s/mm^2 (16 signal averages), half Fourier and targeted shimming (bilateral, i.e., separate shim regions over

each breast, for MB and conventional DWI, matching the prescribed rectangular FOV for reduced-FOV) were used. The scan time for 16 axial slices was 1min. 12sec. for conventional and reduced-FOV DWI and 4min. 50sec. for the proposed MB method.

An experienced radiologist reviewed all images in randomized order during different sessions to enable comparison of diagnostic accuracy between series, while minimizing memory effects. No other information was provided to the radiologist other than the images acquired with the three different pulse sequences. Images were scored for a) level of distortion; b) residual aliasing; c) quality of fat suppression; d) perceived SNR and e) anatomical detail on a 5 point scale (1=worst, 5=best). Statistical significance (set at $p<0.05$) was tested using the Wilcoxon signed-rank test.

Results

Phantom experiments

Figure 2a shows a reference spin echo image acquired with a single-channel head coil and simulated excitation profiles obtained using the MB 2D RF pulse described above. Two "virtual" coil images (middle row) were obtained by multiplying each excitation pattern by the reference image. Each "virtual" coil sees a different part of the object being imaged, so that a generalized parallel imaging method, where each "virtual" coil is treated as if it was a physical receiver coil, can be used to reconstruct retrospectively-undersampled datasets. The bottom row of Figure 2a compares sum-of-squares (top half) and SENSE (bottom half) reconstructions of a 2× undersampled dataset. Artifacts at the boundaries between adjacent bands are barely visible, as expected in the ideal case where sensitivity maps are perfectly known, but with sum-of-squares combination, the expected aliasing appears. In Figure 2b, three excitations, with two simultaneously excited bands, covered the desired FOV. In this case there was almost no difference between this acquisition scheme and that shown in Figure 2a, probably due to the high SNR of the reference spin echo image. As in conventional parallel imaging, the maximum achievable FOV-reduction factor is limited by the number and sensitivities of coils available. Here, in order to successfully reconstruct a 4× undersampled dataset, at least 4 different excitations were necessary, as shown in Figure 2c, to avoid any single band aliasing onto itself. Figure 3 shows images obtained using the same spin-echo acquisition and an 8-channel head coil. Non-MB images were obtained by conventional SENSE reconstruction of retrospectively undersampled datasets. Parallel imaging artifacts were visible for $R = 4$ and became unacceptable for $R = 8$. MB images were obtained by simulating a MB factor of 2, with 3 excitations to cover the desired FOV (cfr. Figure 2b). In this case, 3 (Np) × 8 (Nc) = 24 "virtual" coils successfully resolved aliasing up to $R = 16$, demonstrating that multiple MB excitation patterns can be used to extend the parallel imaging capabilities of conventional coils at the expense of increased acquisition time.

Figure 4 shows covariance matrices for the standard (yellow box) and virtual coil configurations obtained in an 8-channel breast coil using conventional and multiband acquisitions. Note that in the virtual coil configuration, the covariance matrix of the standard configuration is replicated along the diagonal for as many times as the number of passes necessaries to sweep the prescribed FOV. Also note that, by design, the virtual coils

introduced with the multiband acquisition scheme are minimally correlated. This led to an effective g-factor reduction in the multiband case. An alternative way to interpret this result is that for multiband, the number of samples necessary to reconstruct each pass is lower than in the full FOV case, which means that the effective FOV reduction factor and associated g-factor are lower. According to this second interpretation, the multiband reconstruction can be viewed as a two-step process, with the first step consisting in the separation of simultaneously excited bands and the second step being a coil combination problem. According to this formalism, g-factor would be more suitably defined with respect to a hypothetical "non accelerated" acquisition in the multiband sense, obtained for instance by phase cycling the excitation RF pulse and Fourier transformation in the multiband dimension.

In vivo imaging

Figure 5 shows MB and non MB EPI images (b=0) acquired in a healthy volunteer. As ETL was the same for the two acquisitions, so was the resulting point spread function. While both MB and non MB images could be successfully reconstructed up to a FOV reduction factor of 8 (i.e., 8× undersampling), the SNR penalty associated with progressively higher undersampling factors was much more evident in the non-MB images. This is evident from the zoomed view in the lower half of Figure 5, where detail of the left breast of a different volunteer is shown. Due to the progressively higher resolution, the echo spacing is also increasing from left to right. While distortion in EPI is directly proportional to the echo spacing, the relative differences involved are not large enough to result in significant changes in the associated distortion field.

Figure 6 shows b=0 and b=600s/mm^2 images acquired with a MB factor of 2 and a FOV reduction factor of 4 and reconstructed using image-space and *k*-space-based parallel imaging. SENSE-based reconstructions showed more residual aliasing and overall worse image quality than the corresponding ARC-based reconstructions, especially in slices where large amounts of fat tissue were present.

Pilot comparative study in patients

MB, conventional and reduced-FOV DWI images were successfully acquired in all patients. Figures 7 and 8 show bilateral images obtained with MB and conventional DWI as well as reduced-FOV DWI. Overall, no significant difference was observed between MB and reduced-FOV DWI in terms of distortion (p=0.4), quality of fat suppression (p=0.7), perceived SNR (p=0.1) and anatomical detail (p=0.7) (Table 1). Minor residual aliasing was noted in MB but not in reduced-FOV (MB parallel imaging factor = 8 vs. no parallel imaging for reduced-FOV). With respect to conventional DWI, MB images were less distorted (p=0.03) and were found to be superior both in terms of anatomical detail (p=0.02) and fat suppression (p=0.03). Perceived SNR and level of residual aliasing were not significantly different.

Discussion

Parallel imaging remains the most widely used method to reduce distortion and blurring in high-resolution DWI. However, commercially available array coils often limit the maximum FOV-reduction factor achievable with this technique. Readout-segmented methods (7,8,11,13), used in conjunction with parallel imaging, can further reduce distortion by reducing ESP, although longer acquisition times often result from acquiring several blinds separately, and k-space traversal is less efficient due to more frequent reversal of gradients. Here we developed a novel technique that, similarly to readout-segmented methods, can be used in conjunction with conventional parallel imaging techniques to allow reduced distortion at the expense of longer scan times.

Unlike readout-segmented EPI, the proposed method is essentially a single-shot image-segmented technique. In multi-shot methods, a series of k-space segments are acquired following different excitations, causing different motion-induced phase errors to affect different segments. In our MB method, the entire k-space, though undersampled, is acquired following each excitation, so that each shot can be directly Fourier transformed to obtain a *partial* (due to the MB excitation) and *aliased* (due to undersampling) representation of the object being imaged. While different excitations are necessary to sweep the prescribed FOV, meaning that phase inconsistencies are inevitably present between different shots, these are automatically accounted for and compensated by a generalized parallel imaging reconstruction where each of these images is regarded as if it originated from a different receiver coil. In *k*-space based methods coil images are reconstructed separately and then combined using a sum of squares approach. Image-domain methods generally combine the phase information from different coil elements. However, the use of homodyne reconstruction effectively removes unwanted phase inconsistencies in the combined images. Bulk motion between shots can still produce artifacts at the junction between consecutive bands. While compressed breast tissue is almost motion-free, inter-shot motion due to cardiac pulsation and/or breathing is likely to be one of the main factors to be accounted for in abdominal imaging. Conventional motion-compensating strategies like cardiac gating and/or respiratory triggering, as well as the use of navigator echoes should be further investigated for these particular applications. Compared to readout-segmented EPI, the scan efficiency will similarly depend on the number of shots required. Readout-segmented EPI is more SNR efficient, as it benefits from signal averaging, but the proposed method is more efficient in terms of readout efficiency, as it does not require the acquisition of navigator echoes. Specific comparisons between the two techniques would depend on the parameters of each sequence, such as the time to acquire navigator echoes, as well as considerations of slice and pass interleaving.

We demonstrated that if there is enough coil sensitivity variation between simultaneously excited bands, parallel imaging can separate them apart with minimal noise amplification. The same concept applies to simultaneous multi slice imaging where parallel imaging alone can be used to separate simultaneously excited slices, provided that there is enough coil sensitivity variation between them. Techniques like blipped CAIPI (41,42) can separate slices that have essentially the same sensitivity profile by modifying the aliasing pattern between simultaneously excited slices. Here we use a series of multiband excitations to split

each sensitivity profile in a series of profiles that varies more rapidly across the FOV. This allows separation of adjacent bands of magnetisation that would otherwise be difficult to separate due to the almost identical underlying sensitivity profiles.

We have shown that the proposed method can be used for high-resolution DWI of the breast to obtain bilateral coverage with similar resolution and anatomical fidelity as those recently achieved over targeted regions using reduced-FOV methods (30,31). There are other options to use reduced-FOV scans for bilateral breast imaging. The simplest would be to acquire two reduced-FOV scans, one on each breast (note that a multiband approach would make sense even here). However to cover the whole of each breast, the bands would need to be 10–12cm thick, resulting in 2.5 to 3 times the distortion that we have shown. Additionally, it is often important to cover the sternal and axillary regions. Ultimately, to minimize distortion, narrower bands will be needed, and the proposed multiband method will be preferred, as it offers a tradeoff between coverage and efficiency.

In the breast, with a 16 channel receive coil, the maximum FOV-reduction factor was essentially limited by SNR considerations. Line-scan imaging (43), which has been previously proposed for virtually distortion-free DWI and which can be considered as an extreme case of the method proposed here, has found limited applications due to the extremely low SNR involved and long acquisition times. Another potential problem associated with encoding an extremely reduced FOV is the inevitable mismatch between the actual deformation field resulting from the undersampled data and the deformation field associated with the calibration data. If a high enough FOV reduction factor is used, the minimum achievable ESP, as determined by slew rate and gradient strength, often gives larger distortions than the corresponding reduced-FOV acquisition. It has been previously shown that this mismatch can affect the quality of the parallel imaging reconstruction (10). An alternative strategy to acquire calibration data with deformation matched to the actual data consists of acquiring the b=0 images using a multishot approach, with the *k*-space raster shifted by a single line on every new excitation, so as to fully sample *k*-space (44). Because no diffusion gradients are played out, there are no phase inconsistencies between the different segments, and as multiple acquisitions are commonly used in DWI to build SNR, there is no additional time penalty.

It should be noted that both transmit and receive RF inhomogeneities are generally accounted for during reconstruction, as long as they are consistent between calibration and actual acquisition, though some SNR variation may occur. Also, B1 transmit inhomogeneities could be partly compensated by modulating the amplitude of the different bands for each excitation pattern. While this would imply a step-wise modeling of the underlying B1- field along the PE direction, which is often an oversimplification, this approach could significantly reduce B1induced shading, in cases where B1 variations are particularly severe (e.g. breast imaging). A further step could include sloping individual profiles, though the time-bandwidth product used in this work (3.1) may limit the degree of selectivity possible.

One of the main limitations of the proposed MB method is that in order to avoid saturation effects from side lobes of the 2D RF excitation profile, the maximum number of slices per

TR is limited to as many as can fit between two consecutive excitation side lobes (21). While this limitation could be removed by tilting the plane of the excitation gradients to produce staggered side lobes (45), we have recently demonstrated that an alternative time-effective way to increase coverage in the slice direction consists in combining the MB method proposed here with conventional through-slice MB techniques (42,46), where multiple slices are acquired simultaneously (47). By phase modulating the 180º refocusing pulse, multiple excitation lobes can be simultaneously refocused and imaged. A generalized parallel imaging approach, similar to that described here, can be used to resolve in-plane and through-plane aliasing as well as to produce combined images for each slice. It should also be noted that saturation effects could be avoided by using a longer TR and judicious ordering of the excited slices, which may be more time-efficient than performing an entire second acquisition as in ref. (21).

While our MB method has been developed in the context of spin-echo EPI, commonly used for DWI, the acquisition scheme and reconstruction techniques described in this work could be modified for gradient-echo imaging by swapping fast and slow direction during excitation and oversampling in the PE direction (48). In this case, multiple coplanar bands are simultaneously excited due to the discrete sampling of *k*-space in the PE direction. While this design is compatible with gradient echo imaging (no excitation side lobes in the slice direction), additional pulses would be required for fat suppression and the range of MB excitation patterns to choose from would now be bound by RF design considerations.

The fat suppression method used for our multiband technique has been previously described in the context of rFOV DWI by Saritas et al (21). The underlying mechanism is similar to that of other gradient reversal methods used for twice-refocused DWI (49). It relies on the slice-select bandwidth of the excitation RF pulse to be low enough so that fat is shifted outside of the volume refocused by the 180° RF pulse. Off-resonance effects can lead to signal loss due to off-resonant spins also being shifted outside of the refocused volume. It should be noted that off-resonance affects chemical saturation in a similar way, when signal generating from off-resonance water falls within the bandwidth of the saturation pulse. In either case, accurate shimming is crucial to ensure accurate fat suppression.

Careful evaluation of ADC maps, especially in the presence of pathology was beyond the scope of this paper. As an example, Figure 9 shows ADC maps of a healthy breast with the conventional full FOV acquisition and a FOV reduction of 4 (a), with a multiband factor of 3 and the same FOV reduction factor (b) and with a multiband factor of 3 and a FOV reduction factor of 8 (c). FOV was 40cm. Matrix size was 256^2 for (a) and (b) and 512^2 for (c). The inserts on the right show a detail of the right breast. ADC values of healthy fibroglandular tissue were 1.7+/−0.2 (a), 1.7+/−0.3 (b) and 1.6+/−0.4 (c) x10–3 mm^2/s. While no significant artefacts were present in the multiband maps when compared to the conventional map, the high-resolution map (c) was noisier and gave lower ADC with respect to the first two, which could be due to noise floor effects. An additional factor to take into consideration, especially in the presence of pathology, is that high-resolution maps suffer less from partial volume effects due to the smaller voxels, which could lead to an apparent bias in ADC when evaluated on the basis of high-resolution images.

In conclusion, we have developed and shown feasibility of a novel technique for high-resolution DWI that combines 2D in-plane MB RF pulses and a generalized parallel imaging reconstruction method to produce high-resolution DW images with minimal distortion. A preliminary study conducted in patients with known breast lesions showed that the same resolution achievable over targeted regions of limited extent with reduced-FOV methods can be obtained with bilateral coverage and similar overall image quality using the proposed MB method.

Acknowledgements

References

1. Partridge SC, Demartini WB, Kurland BF, Eby PR, White SW, Lehman CD. Differential diagnosis of mammographically and clinically occult breast lesions on diffusion-weighted MRI. J Magn Reson Imaging 2010;31:562–570. [PubMed: 20187198]

2. Ei Khouli RH, Jacobs MA, Mezban SD, Huang P, Kamel IR, Macura KJ, Bluemke DA. Diffusion-weighted imaging improves the diagnostic accuracy of conventional 3.0-T breast MR imaging. Radiology 2010;256:64–73. [PubMed: 20574085]

3. Partridge SC, DeMartini WB, Kurland BF, Eby PR, White SW, Lehman CD. Quantitative diffusion-weighted imaging as an adjunct to conventional breast MRI for improved positive predictive value. AJR Am J Roentgenol 2009;193:1716–1722. [PubMed: 19933670]

4. Bammer R, Keeling SL, Augustin M, Pruessmann KP, Wolf R, Stollberger R, Hartung HP, Fazekas F. Improved diffusion-weighted single-shot echo-planar imaging (EPI) in stroke using sensitivity encoding (SENSE). Magn Reson Med 2001;46:548–554. [PubMed: 11550248]

5. Bogner W, Pinker-Domenig K, Bickel H, Chmelik M, Weber M, Helbich TH, Trattnig S, Gruber S. Readout-segmented echo-planar imaging improves the diagnostic performance of diffusion-weighted MR breast examinations at 3.0 T. Radiology 2012;263:64–76. [PubMed: 22438442]

6. Chen NK, Guidon A, Chang HC, Song AW. A robust multi-shot scan strategy for high-resolution diffusion weighted MRI enabled by multiplexed sensitivity-encoding (MUSE). Neuroimage 2013;72:41–47. [PubMed: 23370063]

7. Heidemann RM, Porter DA, Anwander A, Feiweier T, Heberlein K, Knosche TR, Turner R. Diffusion imaging in humans at 7T using readout-segmented EPI and GRAPPA. Magn Reson Med 2010;64:9–14. [PubMed: 20577977]

8. Holdsworth SJ, Skare S, Newbould RD, Bammer R. Robust GRAPPA-accelerated diffusion-weighted readout-segmented (RS)-EPI. Magn Reson Med 2009;62:1629–1640. [PubMed: 19859974]

9. Liu C, Bammer R, Kim DH, Moseley ME. Self-navigated interleaved spiral (SNAILS): application to high-resolution diffusion tensor imaging. Magn Reson Med 2004;52:1388–1396. [PubMed: 15562493]

10. Skare S, Newbould RD, Clayton DB, Albers GW, Nagle S, Bammer R. Clinical multishot DW-EPI through parallel imaging with considerations of susceptibility, motion, and noise. Magn Reson Med 2007;57:881–890. [PubMed: 17457876]

11. Skare S, Newbould RD, Clayton DB, Bammer R. Propeller EPI in the other direction. Magn Reson Med 2006;55:1298–1307. [PubMed: 16676335]

12. Griswold MA, Jakob PM, Chen Q, Goldfarb JW, Manning WJ, Edelman RR, Sodickson DK. Resolution enhancement in single-shot imaging using simultaneous acquisition of spatial harmonics (SMASH). Magn Reson Med 1999;41:1236–1245. [PubMed: 10371457]

13. Porter DA, Heidemann RM. High resolution diffusion-weighted imaging using readout-segmented echo-planar imaging, parallel imaging and a two-dimensional navigator-based reacquisition. Magn Reson Med 2009;62:468–475. [PubMed: 19449372]

14. Smith TB, Nayak KS. Reduced field of view MRI with rapid, B1-robust outer volume suppression. Magn Reson Med 2012;67:1316–1323. [PubMed: 22083545]

15. von Morze C, Kelley DA, Shepherd TM, Banerjee S, Xu D, Hess CP. Reduced field-of-view diffusion-weighted imaging of the brain at 7 T. Magn Reson Imaging 2010;28:1541–1545. [PubMed: 20850242]

16. Wargo CJ, Gore JC. Localized high-resolution DTI of the human midbrain using single-shot EPI, parallel imaging, and outer-volume suppression at 7T. Magn Reson Imaging 2013;31:810–819. [PubMed: 23541390]

17. Wilm BJ, Svensson J, Henning A, Pruessmann KP, Boesiger P, Kollias SS. Reduced field-of-view MRI using outer volume suppression for spinal cord diffusion imaging. Magn Reson Med 2007;57:625–630. [PubMed: 17326167]

18. Feinberg DA, Hoenninger JC, Crooks LE, Kaufman L, Watts JC, Arakawa M. Inner volume MR imaging: technical concepts and their application. Radiology 1985;156:743–747. [PubMed: 4023236]

19. Jeong EK, Kim SE, Guo J, Kholmovski EG, Parker DL. High-resolution DTI with 2D interleaved multislice reduced FOV single-shot diffusion-weighted EPI (2D ss-rFOV-DWEPI). Magn Reson Med 2005;54:1575–1579. [PubMed: 16254946]

20. Kim SE, Jeong EK, Shi XF, Morrell G, Treiman GS, Parker DL. Diffusion-weighted imaging of human carotid artery using 2D single-shot interleaved multislice inner volume diffusion-weighted echo planar imaging (2D ss-IMIV-DWEPI) at 3T: diffusion measurement in atherosclerotic plaque. J Magn Reson Imaging 2009;30:1068–1077. [PubMed: 19856440]

21. Saritas EU, Cunningham CH, Lee JH, Han ET, Nishimura DG. DWI of the spinal cord with reduced FOV single-shot EPI. Magn Reson Med 2008;60:468–473. [PubMed: 18666126]

22. Zaharchuk G, Saritas EU, Andre JB, Chin CT, Rosenberg J, Brosnan TJ, Shankaranarayan A, Nishimura DG, Fischbein NJ. Reduced field-of-view diffusion imaging of the human spinal cord: comparison with conventional single-shot echo-planar imaging. AJNR Am J Neuroradiol 2011;32:813–820. [PubMed: 21454408]

23. Reischauer C, Wilm BJ, Froehlich JM, Gutzeit A, Prikler L, Gablinger R, Boesiger P, Wentz KU. High-resolution diffusion tensor imaging of prostate cancer using a reduced FOV technique. Eur J Radiol 2011;80:e34–41. [PubMed: 20638208]

24. Rosenkrantz AB, Chandarana H, Pfeuffer J, Triolo MJ, Shaikh MB, Mossa DJ, Geppert C. Zoomed echo-planar imaging using parallel transmission: impact on image quality of diffusion-weighted imaging of the prostate at 3T. Abdom Imaging 2015;40:120–126. [PubMed: 24962196]

25. Thierfelder KM, Scherr MK, Notohamiprodjo M, Weiss J, Dietrich O, Mueller-Lisse UG, Pfeuffer J, Nikolaou K, Theisen D. Diffusion-weighted MRI of the prostate: advantages of Zoomed EPI with parallel-transmit-accelerated 2D-selective excitation imaging. Eur Radiol 2014;24:3233–3241. [PubMed: 25154727]

26. Ma C, Li YJ, Pan CS, Wang H, Wang J, Chen SY, Lu JP. High resolution diffusion weighted magnetic resonance imaging of the pancreas using reduced field of view single-shot echo-planar imaging at 3 T. Magn Reson Imaging 2014;32:125–131. [PubMed: 24231348]

27. Thierfelder KM, Sommer WH, Dietrich O, Meinel FG, Theisen D, Paprottka PM, Strobl FF, Pfeuffer J, Reiser MF, Nikolaou K. Parallel-transmit-accelerated spatially-selective excitation MRI for reduced-FOV diffusion-weighted-imaging of the pancreas. Eur J Radiol 2014;83:1709–1714. [PubMed: 25017152]

28. Jin N, Deng J, Zhang L, Zhang Z, Lu G, Omary RA, Larson AC. Targeted single-shot methods for diffusion-weighted imaging in the kidneys. J Magn Reson Imaging 2011;33:1517–1525. [PubMed: 21591023]

29. Taviani V, Nagala S, Priest AN, McLean MA, Jani P, Graves MJ. 3T diffusion-weighted MRI of the thyroid gland with reduced distortion: preliminary results. Br J Radiol 2013;86:20130022.

30. Wilmes LJ, McLaughlin RL, Newitt DC, Singer L, Sinha SP, Proctor E, Wisner DJ, Saritas EU, Kornak J, Shankaranarayanan A, Banerjee S, Jones EF, Joe BN, Hylton NM. High-resolution diffusion-weighted imaging for monitoring breast cancer treatment response. Acad Radiol 2013;20:581–589. [PubMed: 23570936]

31. Singer L, Wilmes LJ, Saritas EU, Shankaranarayanan A, Proctor E, Wisner DJ, Chang B, Joe BN, Nishimura DG, Hylton NM. High-resolution diffusion-weighted magnetic resonance imaging in patients with locally advanced breast cancer. Acad Radiol 2012;19:526–534. [PubMed: 22197382]

32. Sui Y, Damen FC, Xie K, Zhou XJ. Image Domain Segmented Diffusion Imaging Using A 2D Excitation RF Pulse for Distortion Reduction. In Poceedings of the 23rd Annual Meeting of ISMRM, Milan, Italy, 2014. p 608.

33. Van AT, Aksoy M, Holdsworth SJ, Kopeinigg D, Vos SB, Bammer R. Slab profile encoding (PEN) for minimizing slab boundary artifact in three-dimensional diffusion-weighted multislab acquisition. Magn Reson Med 2015;73:605–613. [PubMed: 24691843]

34. Pruessmann KP, Weiger M, Scheidegger MB, Boesiger P. SENSE: sensitivity encoding for fast MRI. Magn Reson Med 1999;42:952–962. [PubMed: 10542355]

35. Brau AC, Beatty PJ, Skare S, Bammer R. Comparison of reconstruction accuracy and efficiency among autocalibrating data-driven parallel imaging methods. Magn Reson Med 2008;59:382–395. [PubMed: 18228603]

36. Griswold MA, Jakob PM, Heidemann RM, Nittka M, Jellus V, Wang J, Kiefer B, Haase A. Generalized autocalibrating partially parallel acquisitions (GRAPPA). Magn Reson Med 2002;47:1202–1210. [PubMed: 12111967]

37. Skare S, Clayton DB, Newbould RD, Moseley ME, Bammer R. A fast and robust minimum entropy based ghost correction. In Proceedings of the 14th Annual Meeting of ISMRM, Seattle, USA, 2006. p 2349.

38. King KF, Angelos L. SENSE with partial Fourier homodyne reconstruction. In Proceedings of the 8th Annual Meeting of ISMRM, Denver, USA, 2000. p 153.

39. Robson PM, Grant AK, Madhuranthakam AJ, Lattanzi R, Sodickson DK, McKenzie CA. Comprehensive quantification of signal-to-noise ratio and g-factor for image-based and k-space-based parallel imaging reconstructions. Magn Reson Med 2008;60:895–907. [PubMed: 18816810]

40. Saranathan M, Rettmann DW, Hargreaves BA, Clarke SE, Vasanawala SS. DIfferential Subsampling with Cartesian Ordering (DISCO): a high spatio-temporal resolution Dixon imaging sequence for multiphasic contrast enhanced abdominal imaging. J Magn Reson Imaging 2012;35:1484–1492. [PubMed: 22334505]

41. Breuer FA, Blaimer M, Heidemann RM, Mueller MF, Griswold MA, Jakob PM. Controlled aliasing in parallel imaging results in higher acceleration (CAIPIRINHA) for multi-slice imaging. Magn Reson Med 2005;53:684–691. [PubMed: 15723404]

42. Setsompop K, Gagoski BA, Polimeni JR, Witzel T, Wedeen VJ, Wald LL. Blipped-controlled aliasing in parallel imaging for simultaneous multislice echo planar imaging with reduced g-factor penalty. Magn Reson Med 2012;67:1210–1224. [PubMed: 21858868]

43. Finsterbusch J, Frahm J. Diffusion-weighted single-shot line scan imaging of the human brain. Magn Reson Med 1999;42:772–778. [PubMed: 10502767]

44. Holdsworth SJ, Aksoy M, Newbould RD, Yeom K, Van AT, Ooi MB, Barnes PD, Bammer R, Skare S. Diffusion tensor imaging (DTI) with retrospective motion correction for large-scale pediatric imaging. J Magn Reson Imaging 2012;36:961–971. [PubMed: 22689498]

45. Banerjee S, Saritas EU, Melkus G, Shankaranarayan A. Tilted 2D RF Excitation with Extended Slice Coverage for High-Resolution Reduced-FOV DWI. In Proceedings of the 21st Annual Meeting of ISMRM, Salt Lake City, Utah, USA, 2013. p 57.

46. Larkman DJ, Hajnal JV, Herlihy AH, Coutts GA, Young IR, Ehnholm G. Use of multicoil arrays for separation of signal from multiple slices simultaneously excited. J Magn Reson Imaging 2001;13:313–317. [PubMed: 11169840]

47. Taviani V, Banerjee S, Daniel BL, Vasanawala SV, Hargreaves BA. Two-Dimensional Multiband Diffusion Weighted Imaging. In Proceedings of the 24th Annual Meeting of ISMRM, Toronto, Canada, 2015.

48. Finsterbusch J. Simultaneous functional MRI acquisition of distributed brain regions with high temporal resolution using a 2D-selective radiofrequency excitation. Magn Reson Med 2015;73:683–691. [PubMed: 24574142]

49. Nagy Z, Weiskopf N. Efficient fat suppression by slice-selection gradient reversal in twice-refocused diffusion encoding. Magn Reson Med 2008;60:1256–1260. [PubMed: 18956422]
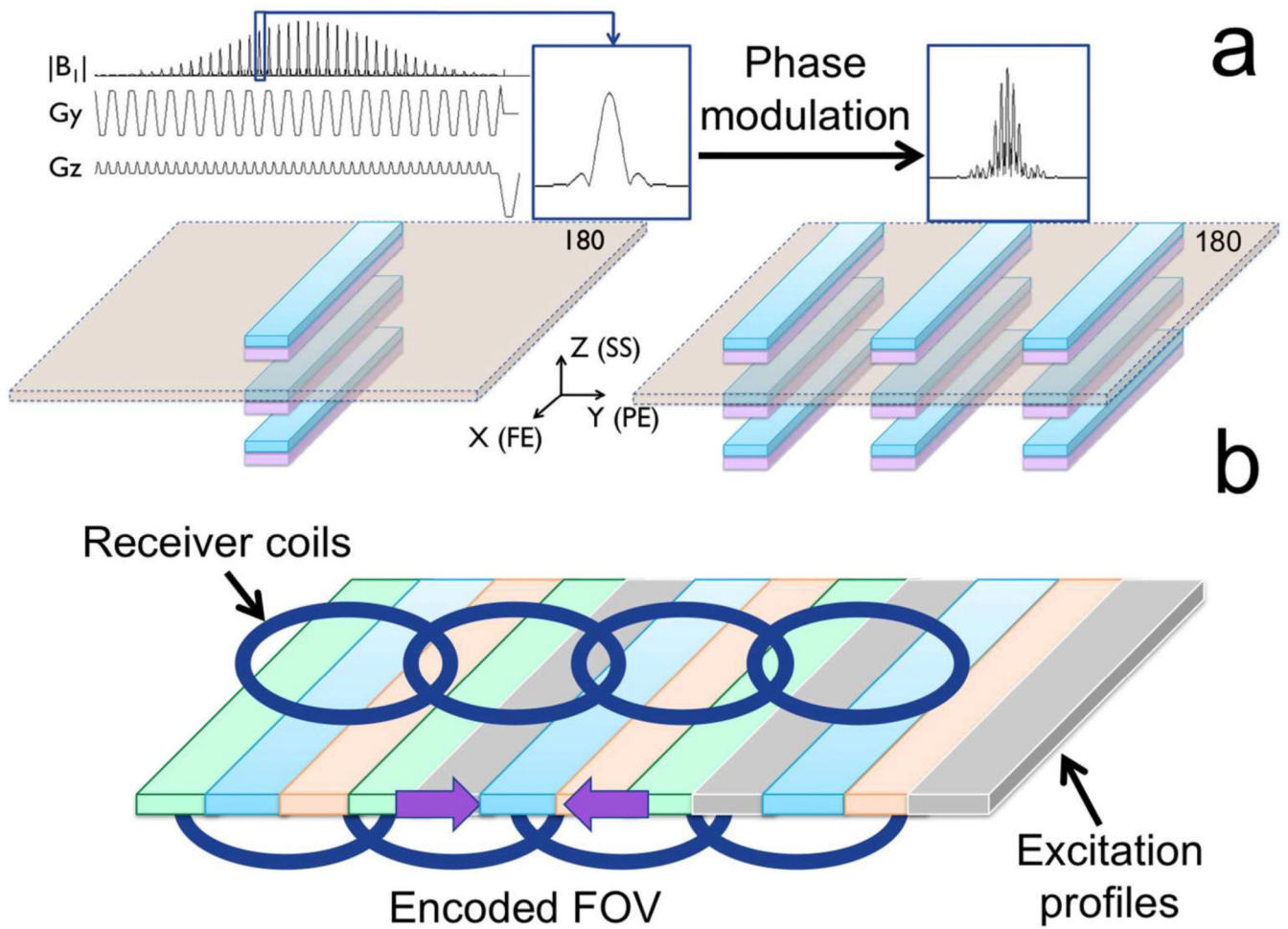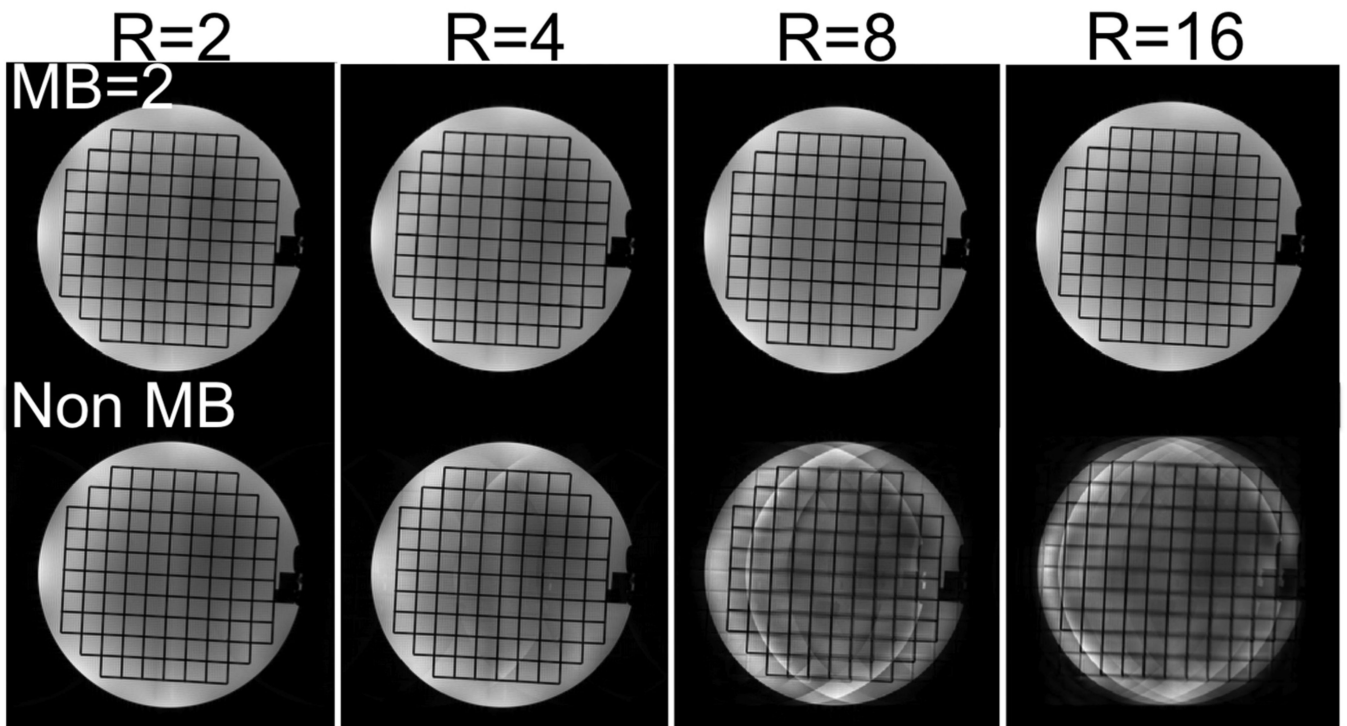
Figure 1.
(a) A 2D RF pulse excites a series of narrow bands of magnetization. If the blipped direction during excitation coincides with the slice-select direction during imaging, each band belongs to a different slice. Due to its chemical shift, fat (purple) is displaced in the slice direction so that refocusing the main water (cyan) excitation lobe alone ensures suppression of unwanted signals originating from fat and other excitation side lobes. By phase modulating the individual sub-pulses, multiple coplanar bands can be simultaneously excited within each slice. (b) The effectively encoded FOV cover the width of a single band. Multiple excitations, with the same MB pattern shifted in the PE direction on each new excitation, are used to cover the prescribed FOV. If the distance between the bands is comparable to the distance between the physical receiver elements of a multichannel array coil, signals originating from different bands can be resolved using parallel imaging.
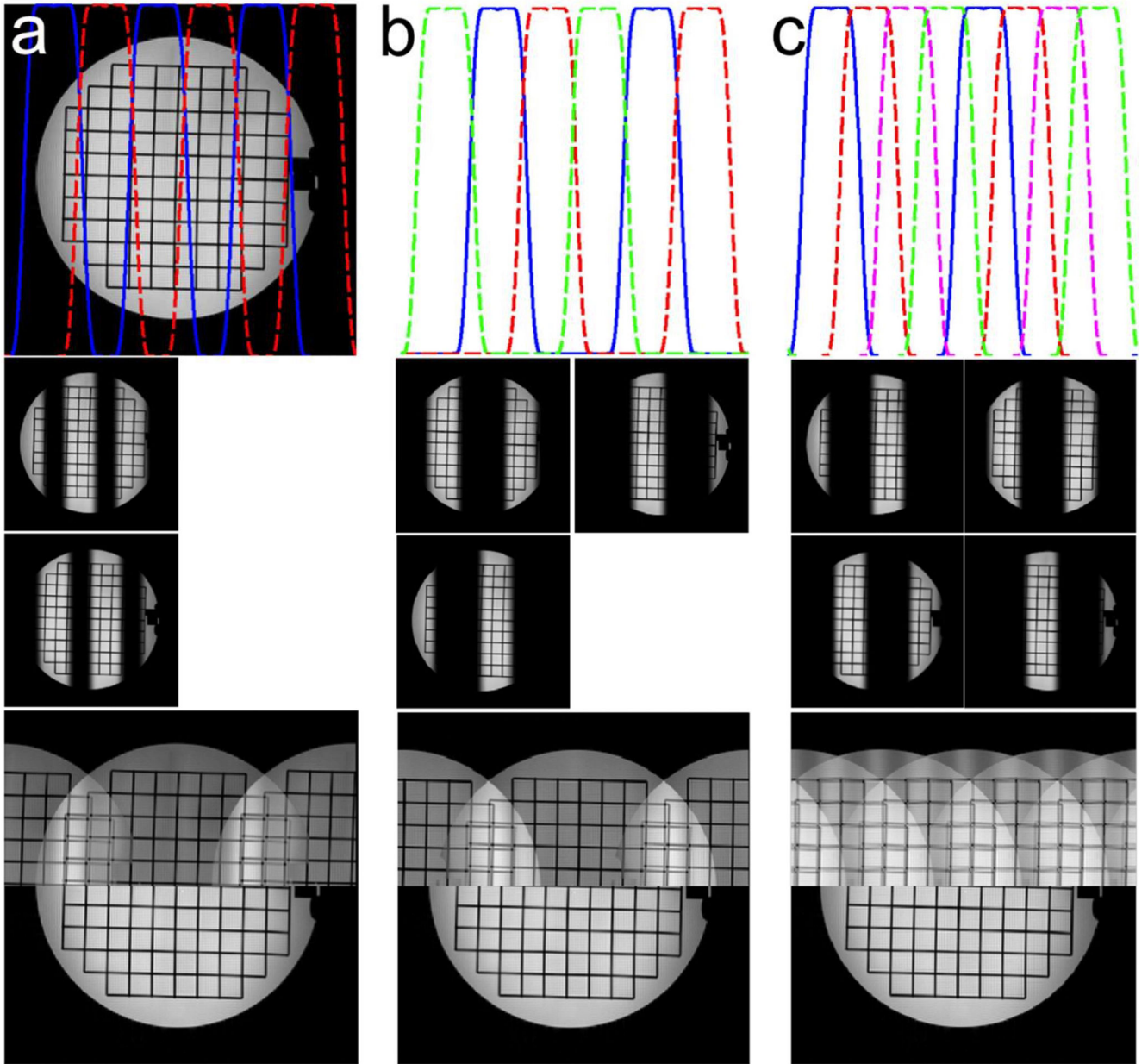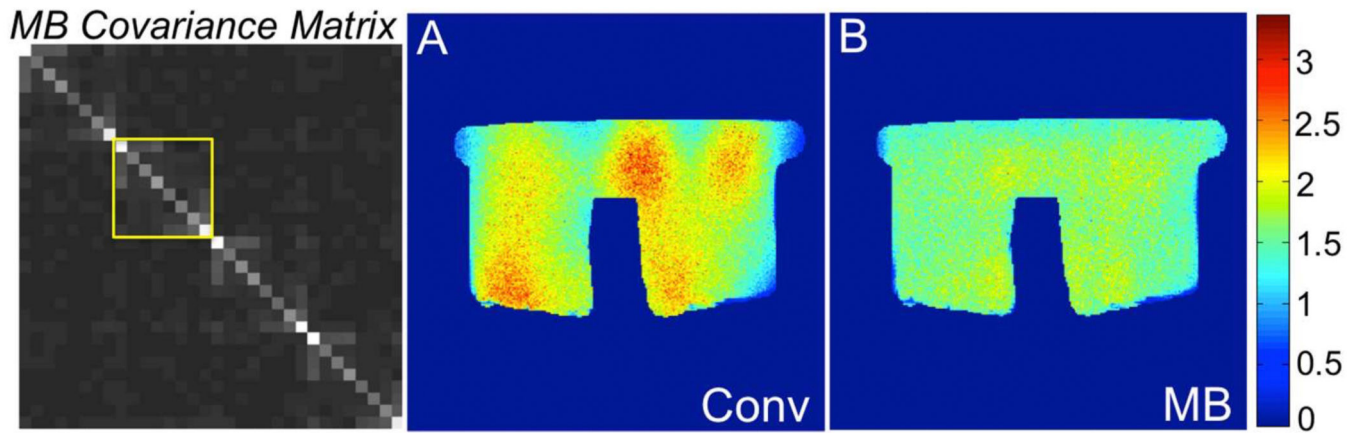
Figure 2.
Top row: reference spin echo image and simulated excitation profiles for: multiband (MB) factor = 3 with 2 excitations (a), MB factor = 2 with 3 excitations (b) and MB factor = 2 with 4 excitations (c). *Middle row*: corresponding "virtual" coil images (as many as the number of excitations necessary to sweep the whole FOV) obtained by multiplying the reference spin echo image and each excitation profile. *Bottom row*: each virtual coil image is undersampled (R = 2 (a), 2 (b) and 4 (c)) and reconstructed by performing a simple inverse Fourier transform followed by sum of squares (*top half*) and by using the proposed generalized SENSE reconstruction (*bottom half*).

Figure 3.

MB (*top row*) and non-MB reconstructions (*bottom row*) of retrospectively undersampled spin echo datasets acquired with an 8-channel receive-only head coil using generalized and conventional SENSE. The use of MB in conjunction with parallel imaging allows greater FOV reduction factors than parallel imaging alone.
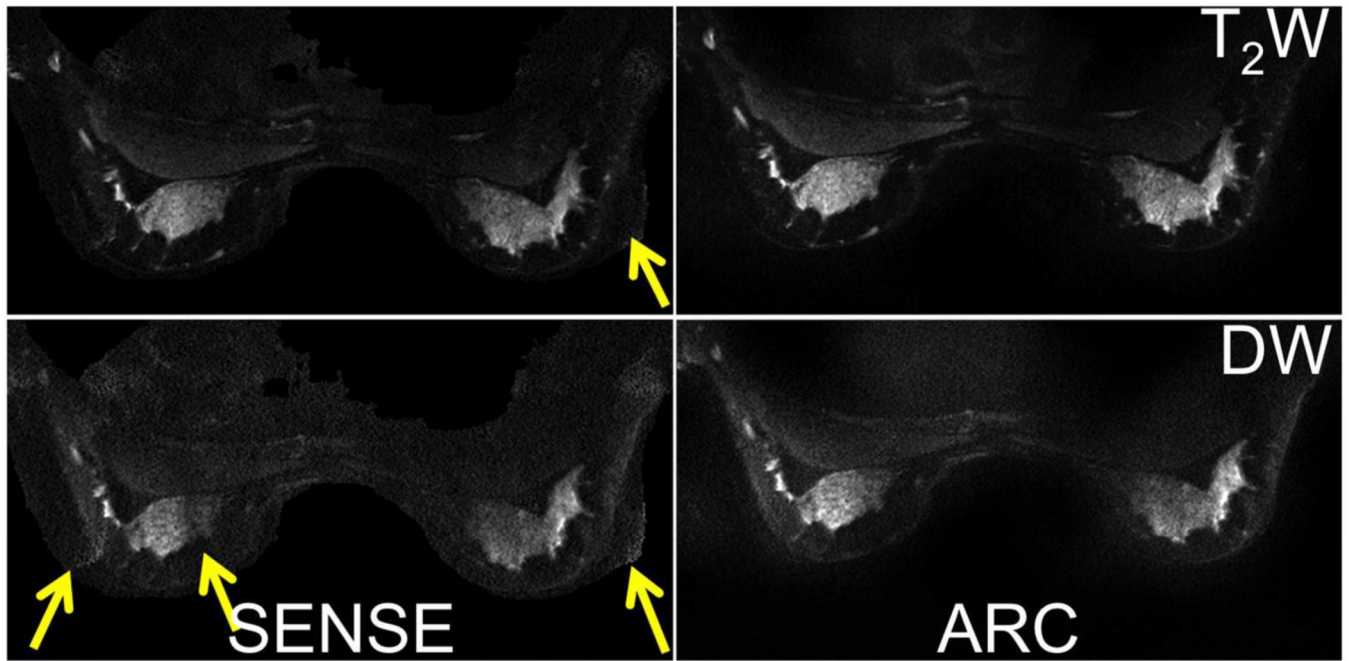
Figure 4.
Noise covariance matrices for standard and virtual coil configurations obtained using an 8-channel breast coil with conventional and multiband acquisitions, respectively. The noise covariance matrix of the standard coil configuration is replicated along the diagonal of the covariance matrix for the virtual coil configuration as many times as the number of passes necessary to sweep the required FOV. As a result, g-factor is on average lower for multiband (b) than for the conventional, full-FOV acquisition (a).
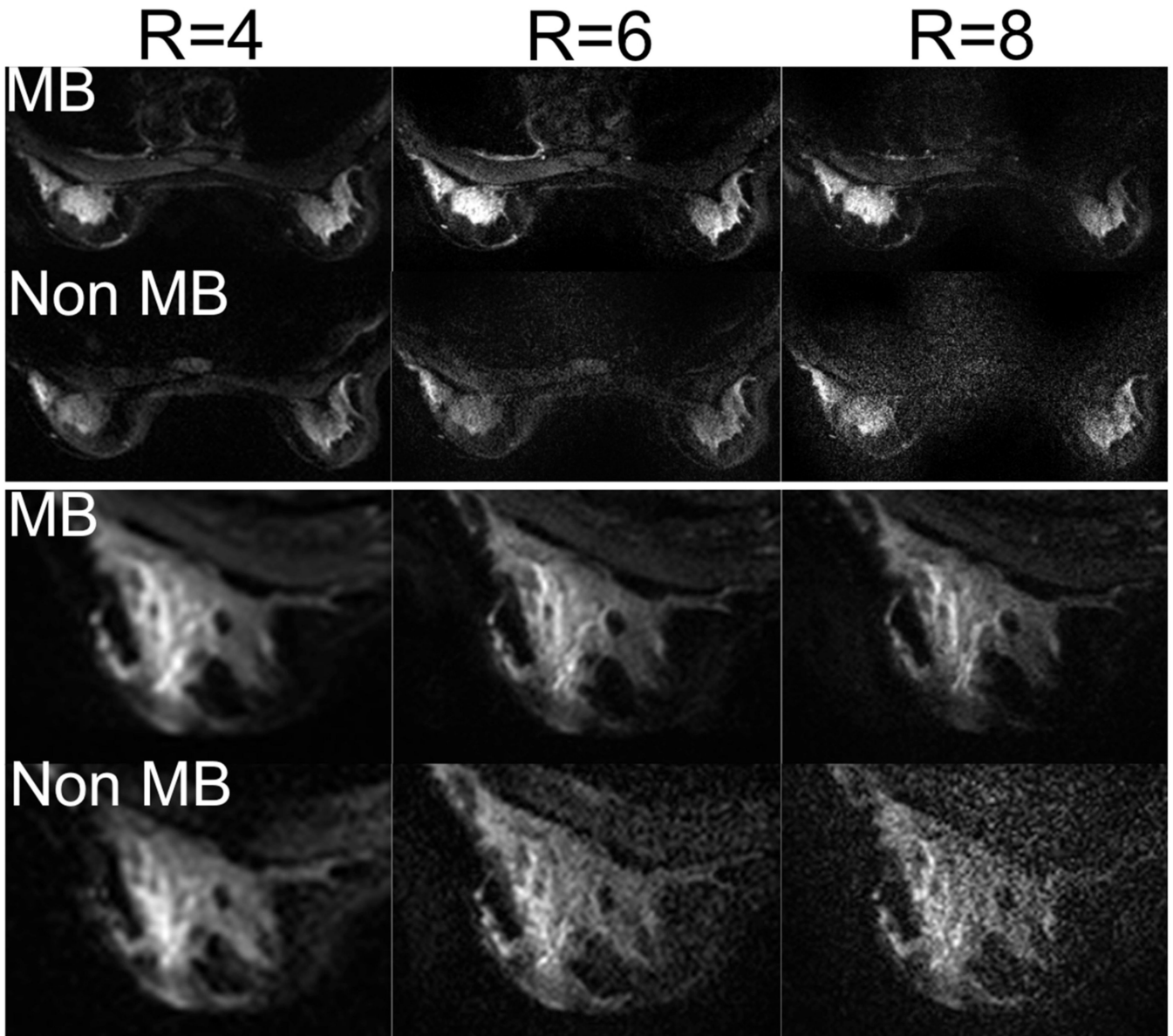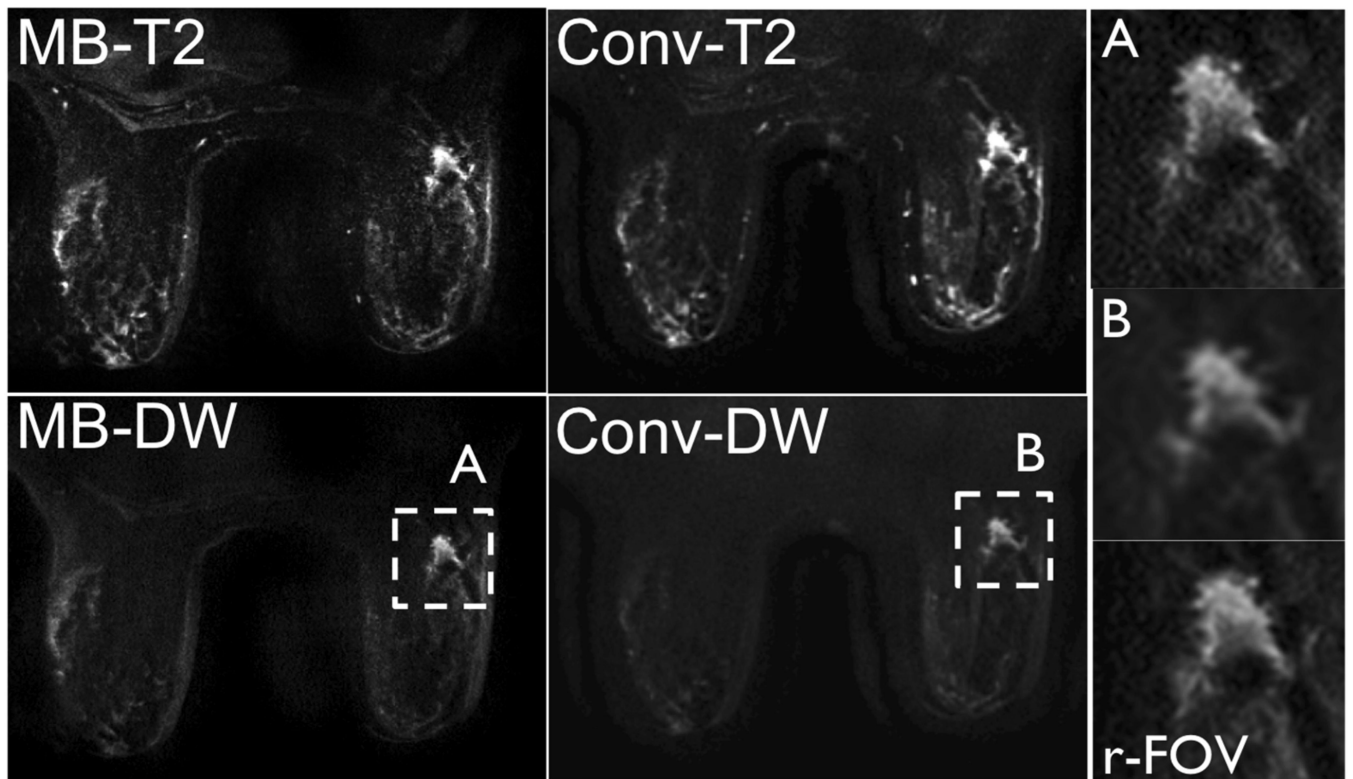
Figure 5.
MB and non-MB images acquired in a healthy volunteer with different FOV reduction factors while varying resolution to maintain the same echo train length (ETL). By progressively reducing the effectively encoded FOV, it is possible to obtain progressively higher resolution images while maintaining the same level of off-resonance-induced distortion and blurring (cfr. close up view of right breast). At higher FOV reduction factors, non-MB images are non-diagnostic due to noise amplification effects. By using MB together with conventional parallel imaging reduces these effects, allowing higher undersampling factors than using parallel imaging alone.
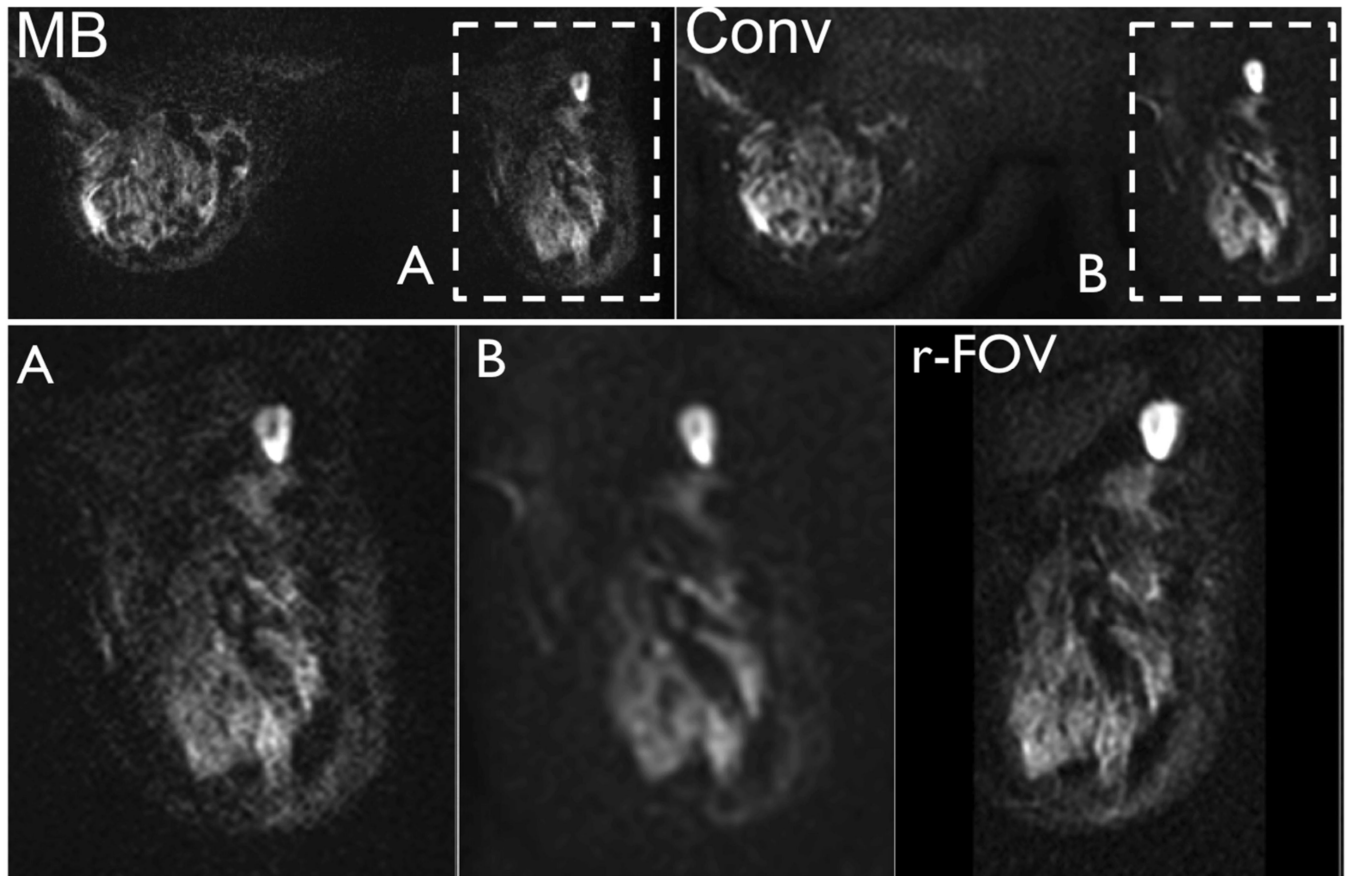
Figure 6.
Generalized SENSE and ARC reconstructions of MB images acquired in a healthy volunteer, with arrows showing residual aliasing in the SENSE reconstructions.
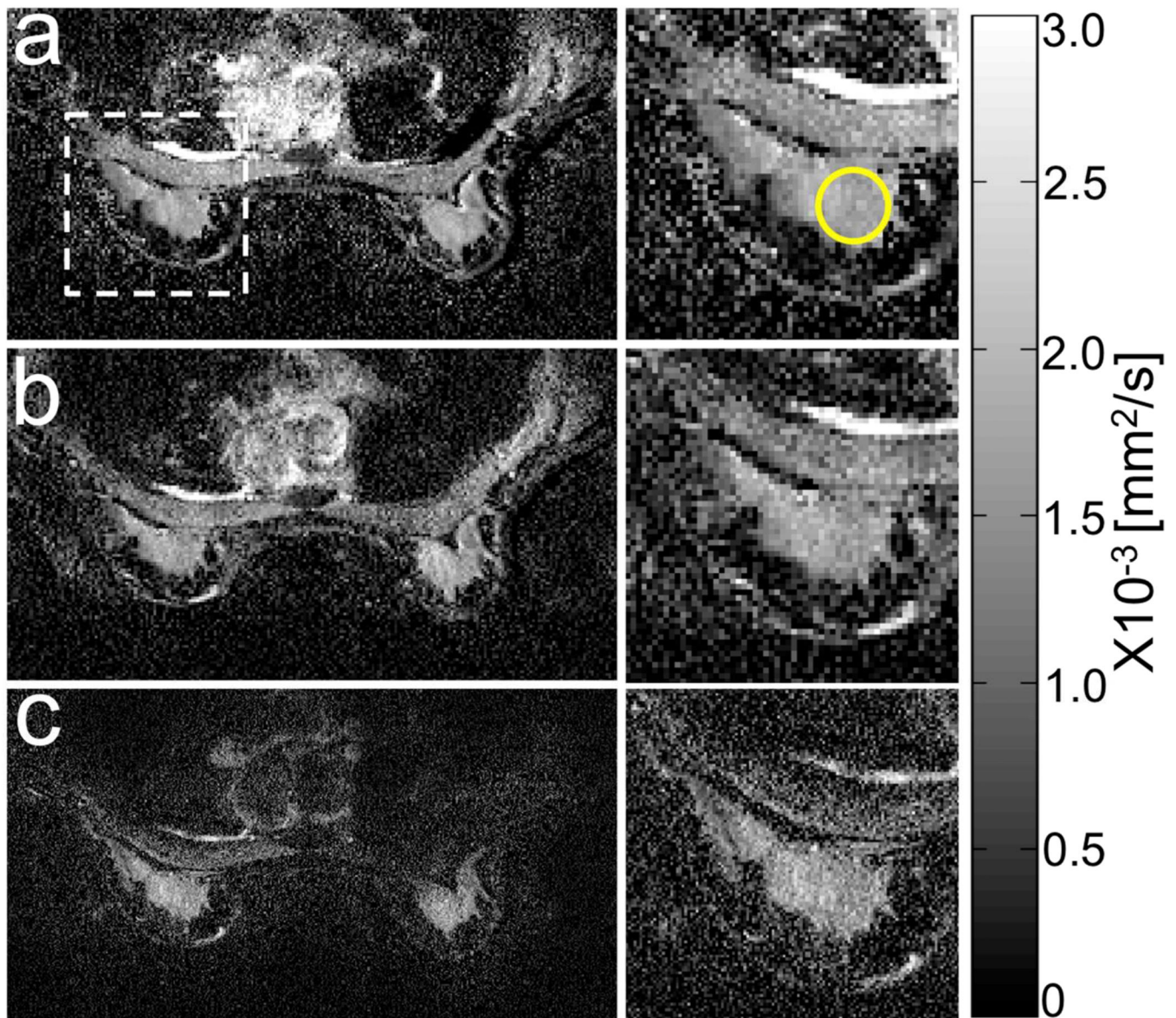
Figure 7.
b = 0 and b = 600s/mm^2 images acquired in a 68 year old patient with invasive ductal carcinoma (right breast, 1.6×1.2×1.0cm^3) using MB and non-MB DWI. Note the similar distortion field between the MB and non-MB acquisitions and the increased resolution achieved with MB (insert A), similar to that achieved using a targeted reduced-FOV method (r-FOV), with respect to non-MB (insert B).

Figure 8.
b = 600s/mm^2 images acquired in a 46 year old patient with right breast invasive ductal carcinoma (1.5cm) and associated extensive (>25%) DCIS (ductal carcinoma in situ), using MB and non-MB DWI. Note the similar distortion field between MB and non-MB images and the increased resolution achieved with MB (insert A) with respect to non-MB (insert B). The same resolution achieved using a targeted reduced-FOV method (r-FOV) is obtained with whole bilateral coverage using the proposed MB method.

Figure 9.
Example of ADC maps in the breast of a healthy volunteer acquired with the conventional full FOV acquisition and a FOV reduction factor of 4 (a), a multiband (MB) factor of 3 and the same FOV reduction factor (b) and a MB factor of 3 and a FOV reduction factor of 8. FOV was 40cm while matrix size was 256^2 for (a) and (b) and 512^2 for (c). The inserts on the right show a detail of the right breast. ADC values of healthy fibroglandular tissue (circular ROI) were 1.7+/−0.2 (a), 1.7+/−0.3 (b) and 1.6+/−0.4 (c) x10–3 mm^2/s. While no significant artefacts were present in the multiband maps when compared to the conventional one, the high-resolution map (c) was noisier and gave a lower ADC with respect to the first two, which could be due to noise floor effects.

Table 1:

Average scores (± standard deviation) for the preliminary patient study (N=14). Conv: conventional bilateral DWI with full FOV excitation; r-FOV: reduced-FOV DWI; MB: multiband DWI.

	Distortion	Aliasing	Fat Sat	SNR	Detail
Conv	3.71 ± 0.82	4.21 ± 0.80	3.57 ± 0.85	3.5 ± 0.65	3.64 ± 0.63
r-FOV	4.64 ± 0.5	4.92 ± 0.27	4.36 ± 0.74	3.57 ± 0.85	4.14 ± 0.66
MB	4.36 ± 0.74	4.07 ± 0.83	4.21 ± 0.58	3.07 ± 0.61	4.28 ± 0.47